Nonequilibrium quantum mechanics: A "hot quantum soup" of paramagnons

H. D. Scammell and O. P. Sushkov
School of Physics, The University of New South Wales, Sydney NSW 2052, Australia
(Received 18 May 2016; revised manuscript received 13 October 2016; published 20 January 2017)

Motivated by recent measurements of the lifetime (decay width) of paramagnons in quantum antiferromagnet $TlCuCl_3$, we investigate paramagnon decay in a heat bath and formulate an appropriate quantum theory. Our formulation can be split into two regimes: (i) a nonperturbative, "hot quantum soup" regime where the paramagnon width is comparable to its energy; (ii) a usual perturbative regime where the paramagnon width is significantly lower than its energy. Close to the Neel temperature, the paramagnon width becomes comparable to its energy and falls into the hot quantum soup regime. To describe this regime, we develop a new finite frequency, finite temperature technique for a nonlinear quantum field theory; the "golden rule of quantum kinetics." The formulation is generic and applicable to any three-dimensional quantum antiferromagnet in the vicinity of a quantum critical point. Specifically, we apply our results to $TlCuCl_3$ and find agreement with experimental data. Additionally, we show that logarithmic running of the coupling constant in the upper critical dimension changes the commonly accepted picture of the quantum disordered and quantum critical regimes.

DOI: 10.1103/PhysRevB.95.024420

I. INTRODUCTION

Understanding the interplay between thermal and quantum fluctuations in quantum systems is an exciting challenge to theory. In particular, understanding how to appropriately treat (quasi)particles in a hot and dense medium is of fundamental importance to many areas of physics ranging from condensed matter, to plasma, nuclear, and particle physics. In this work we concentrate on the lifetimes of quasiparticles, or, more generally, on the line shapes of spectral functions. The lifetime and the spectral function are essentially nonequilibrium properties in spite of the fact that the entire many-body system that we consider is in thermal equilibrium. A perturbative treatment of quasiparticles in a hot dense medium becomes plagued by infrared divergences that occur due to the medium. In this paper, we develop and present a relatively simple technique that (i) regulates the infrared behavior via a resummation of medium effects, i.e., the self-consistent inclusion of line shapes, and (ii) allows one to handle the calculation of nonequilibrium responses at finite temperature.

The problem we investigate was stimulated by the observation of paramagnons in the magnetically disordered phase of the three-dimensional (3D), dimerized quantum antiferromagnet $TlCuCl_3$ [1]. The pressure-temperature phase diagram of the compound is shown in Fig. 1. The quantum phase transition at the quantum critical point (QCP) $p = p_c = 1.01$ kbar is driven by external hydrostatic pressure. The red line in Fig. 1 shows the Néel temperature versus pressure [2]. At $p > p_c$ and temperatures below the Néel curve, the compound possesses long-range antiferromagnetic order. Going above the Néel curve at $p > p_c$, the system becomes magnetically disordered, while at $p < p_c$ the system is disordered even at zero temperature. Magnetic excitations at zero temperature and at $p < p_c$ are usually called triplons, while magnetic excitations at $p > p_c$ and $T > T_N$ are usually called paramagnons. It is clear from Fig. 1 that there is no qualitative difference between triplons and paramagnons and so throughout this work we will exclusively use the term paramagnon, i.e, a triplon is a paramagnon.

It was observed [1,2] that at temperatures just above the Néel temperature T_N, the paramagnons are relatively broad, $\Gamma/\omega \gtrsim 1$, here Γ is the width and ω is the energy of the paramagnon. At increasing temperatures, the paramagnons become narrow, $\Gamma/\omega \ll 1$. This unexpected behavior is an indication of a nontrivial interplay between quantum and thermal fluctuations [3].

While $TlCuCl_3$ is a spin dimerized compound, the phase diagram in Fig. 1 is essentially the generic phase diagram of a 3D isotropic quantum antiferromagnet [4], dimerized or not. The widths of magnons in the magnetically ordered phase of quantum magnets have received both theoretical and experimental attention [5–9]. On the other hand, we are not aware of any previous theoretical studies of decay widths of paramagnons in the disordered phase of 3D quantum antiferromagnets at finite temperatures.

In the magnetically ordered phase at low temperatures, $T < T_N$, there exists two types of magnetic excitations. First, there are Goldstone excitations called magnons. Magnons are generally long lived quasiparticles which weakly interact with each other [5–8]. This holds especially true for higher-dimensional, nonfrustrated systems, or systems without spontaneous decay [9]. The long lifetime of magnons, $\Gamma/\omega \ll 1$, is due to Adler's theorem, which claims that the magnon-magnon interaction must vanish in the long-wavelength limit. Adler's theorem is a general dynamic property unrelated to the magnitude of the effective coupling constant. Also within the magnetically ordered phase, along with the Goldstone magnons, there exist longitudinal (Higgs) magnetic excitations. The width of Higgs excitations depends on the magnitude of the effective coupling constant, and is not governed by Adler's theorem. It can be large, $\Gamma/\omega \gtrsim 1$, like in the Heisenberg model on a simple square or cubic lattice, or it can be small, $\Gamma/\omega \ll 1$, like in $TlCuCl_3$ [10] and some other dimerized spin systems.

In the present work we develop, and subsequently apply, a technique to calculate widths of paramagnons in the magnetically disordered phase of a 3D quantum system in the vicinity of a QCP. While specifically we discuss an O(3) field theory (and apply to the real compound $TlCuCl_3$), the

developed techniques are generic and are applicable to all systems of this kind—the symmetric phases described by O(N)-field theories. For example, they are applicable to the electroweak phase transition in cosmology, to the wide class of spin dimerized magnetic models [11], and to O(2) superfluids or superconductors in the vicinity of their QCP's.

The paper is organized as follows. In Sec. II, we introduce the necessary mathematical and physical techniques. Section III provides an intuitive picture of the decay and scattering processes, with particular focus on the influence of a heat bath. Section IV addresses quantum disordered and quantum critical regimes. We show that they are somewhat different from the commonly accepted picture. Section V discusses the inconsistency of the usual perturbative Fermi golden rule, and introduces our proposed golden rule of quantum kinetics, which simultaneously incorporates decay and heat bath scattering processes, as well as providing a self-consistent, nonequilibrium technique to calculate widths. A general mathematical analysis of the golden rule of quantum kinetics, without reference to any particular system, is given in Sec. VI. Finally, in Sec. VII, we apply our technique to the specific compound $TlCuCl_3$, and compare our results with inelastic neutron scattering experimental data.

II. GENERAL CONSIDERATIONS

In the vicinity of the quantum critical point, quantum antiferromagnets are described by the Landau-Ginzburg-like effective field theory [4,12]

$$\mathcal{L} = \tfrac{1}{2}\partial_\mu\vec{\varphi}\partial^\mu\vec{\varphi} - \tfrac{1}{2}m_0^2\vec{\varphi}^2 - \tfrac{1}{4}\alpha_0\vec{\varphi}^4, \tag{1}$$

where $\vec{\varphi} = (\varphi_1,\varphi_2,\varphi_3)$ is a three-component real vector field describing the spin $S = 1$ magnetic excitations. The index, $\mu = 0,x,y,z$, enumerates time and three-space coordinates, and the paramagnon speed is set equal to unity, $c = 1$. The bare coupling constant is α_0, and the bare effective mass squared m_0^2 changes sign at the QCP, $m_0^2 = \gamma^2(g_c - g)$, where g is some external parameter and γ is a coefficient. For example, in $TlCuCl_3$, the transition is driven by external pressure, $m_0^2 = \gamma^2(p_c - p)$. Below we use the rescaled coupling constant,

$$\beta = \frac{\alpha}{8\pi}, \tag{2}$$

it is a more natural combination for perturbation theory. To apply perturbation theory and the renormalization group (RG), we assume that $\beta \ll 1$. This is always true in a sufficiently close vicinity of the QCP. Quantum and thermal fluctuations lead to running of both the coupling constant and the effective mass; they become energy, momentum, and temperature dependent, $\beta_0 \to \beta_q, m_0^2 \to m_q^2$. Equations for these quantities, derived in Ref. [13], are valid everywhere in the phase diagram in Fig. 1. In the present work, we calculate the width and spectral function of paramagnons within the magnetically disordered region of the phase diagram, Fig. 1.

As a mathematical object we use the retarded Green's function of the paramagnon, which is an analytic continuation of the Matsubara Green's function from the upper imaginary energy half-axis to the real energy axis. To have a coherent presentation, we remind here the basic properties of the retarded Green's function $G^R(\omega,q)$, see, e.g., Ref. [14]. For

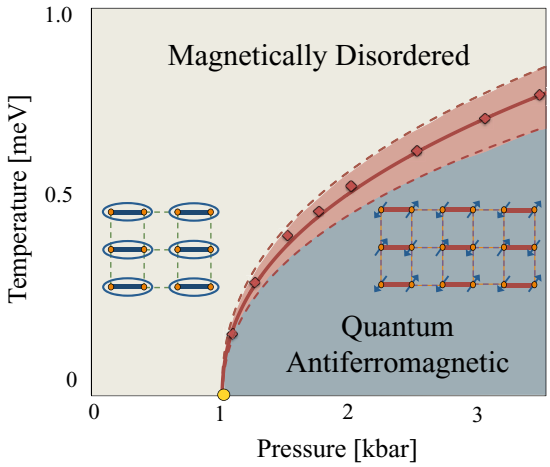

FIG. 1. The pressure-temperature phase diagram of $TlCuCl_3$. The QCP is at $p = p_c = 1.01$ kbar. The Néel temperature curve separates magnetically ordered and magnetically disordered phases. The light red band around the Néel curve indicates the region of dimensional crossover.

the case of a noninteracting field, $\beta = 0$, the Lagrangian (1) becomes

$$\mathcal{L} = \tfrac{1}{2}\partial_\mu\vec{\varphi}\partial^\mu\vec{\varphi} - \tfrac{1}{2}m_0^2\vec{\varphi}^2, \tag{3}$$

and the exact Green's function is immediately deduced:

$$G^R(\omega,\mathbf{q}) = \frac{1}{2\omega_q}\left(\frac{1}{\omega - \omega_q + i0} - \frac{1}{\omega + \omega_q + i0}\right)$$
$$\omega_q = \sqrt{q^2 + m_0^2}. \tag{4}$$

This is true for both zero and nonzero temperatures, as soon as there is no interaction. From (4), we see the symmetry properties of G^R, the real part of G^R is an even function of ω while the imaginary part of G^R is odd. These are general properties valid also in the case of nonzero interaction.

The general spectral representation of G^R follows, see Ref. [14],

$$iG^R(x,0) = \frac{1}{3}\sum_{nm}\frac{e^{-E_n/T}}{Z}e^{-i\omega_{mn}t + i\boldsymbol{k}_{mn}\cdot\boldsymbol{r}}$$
$$\times(1 - e^{-\omega_{mn}/T})|\langle m|\varphi_i(0)|n\rangle|^2. \tag{5}$$

Here, $|n\rangle$ and $|m\rangle$ are exact stationary quantum states of the system, E_n and $\boldsymbol{k}_n$ are the energy and the momentum of the state, $\omega_{mn} = E_m - E_n$, $\boldsymbol{k}_{mn} = \boldsymbol{k}_m - \boldsymbol{k}_n$, while Z is the partition function.

Now consider the interaction of some external source J_i, with the paramagnon field φ_i (for instance J_i can be the magnetic field of a neutron scattered from the system),

$$\mathcal{L}_{\text{int}} = J_i\varphi_i. \tag{6}$$

Assuming that this interaction is very weak, the probability W of the system excitation per unit time, due to interaction with the external source (6), is given by the Fermi golden rule:

$$W \propto S_{\boldsymbol{q}}(\omega) = \frac{1}{3}\sum_{nm}\frac{e^{-E_n/T}}{Z}|\langle m|\varphi_\alpha(0)|n\rangle|^2$$
$$\times\delta(\omega - \omega_{mn})(2\pi)^3\delta(\boldsymbol{q} - \boldsymbol{k}_{mn}). \tag{7}$$

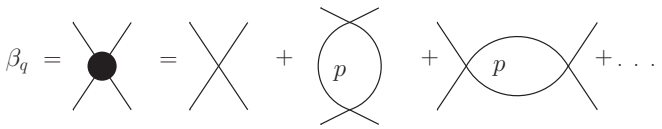

FIG. 2. Diagrammatic subseries: coupling constant.

Here, ω is the energy transfer and $\boldsymbol{q}$ is the momentum transfer to the system. So a scattering experiment allows one to measure the structure factor $S_{\boldsymbol{q}}(\omega)$ defined by Eq. (7). Comparison of Eqs. (5) and (7) results in the following, important, exact relation:

$$-\frac{1}{\pi} Im\ G^R(\omega,\boldsymbol{q}) = (1-e^{-\omega/T}) S_{\boldsymbol{q}}(\omega)\ . \tag{8}$$

Note that Eqs. (5), (7), and (8) are exact, they are valid at arbitrary interaction and arbitrary temperature. Another exact theorem immediately follows from these equations; the imaginary part of $G^R(\omega,\boldsymbol{q})$ is an odd function of ω as already pointed out above.

Account of interaction $\alpha_0\vec{\varphi}^4/4$ in Eq. (1) leads to a paramagnon self-energy $\Sigma_q(\omega)$. Of course, the self-energy depends on temperature, however, for ease of notation we do not write temperature as an explicit argument. The real part of the self-energy has been calculated earlier using the single loop renormalization group (RG) [13]. Account of the real part leads to the replacement $m_0^2 \to m_q^2$ in Eq. (4), where $m_q \equiv \Delta$ is the renormalized mass, such that the dispersion is given by

$$\omega_q = \sqrt{q^2+\Delta^2}\ . \tag{9}$$

Generally, Δ depends on momentum and temperature. Below, we take ω_q as given by Eq. (9). It is important to understand the structure of diagrams included in the self-energy. The diagrams contributing to the running coupling constant β_q are shown schematically in Fig. 2. The momentum in the loop runs in the limits $\Lambda_0 > p > q$, where q is the external momentum and Λ_0 is the ultraviolet cutoff. The self-energy is given by diagrams shown schematically in Fig. 3. All diagrams are quadratically, ultraviolet divergent. Quadratic divergences have no physical meaning and are removed during the renormalization. After removal of the quadratic divergence, the typical momentum in the "external" loop is $k \sim \Delta, T$ while the typical momentum in the "internal" loop is $\Lambda_0 > p > \Delta, T$. The internal loops of the double loop diagrams are inside dashed boxes in Figs. 3(b) and 3(c). The series of internal loops can be identified as the series of the running coupling constant, as shown in Fig. 2. The point to note is that the most important logarithmically divergent part of the "sunset" diagram (see Fig. 6, considered in the next section) is fully included in our RG calculation of Δ [13].

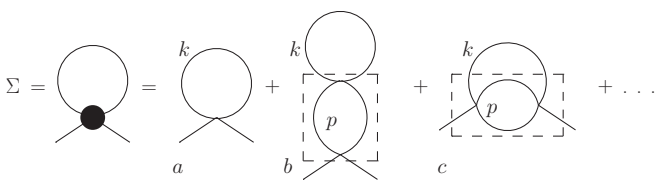

FIG. 3. Diagrammatic subseries: self-energy.

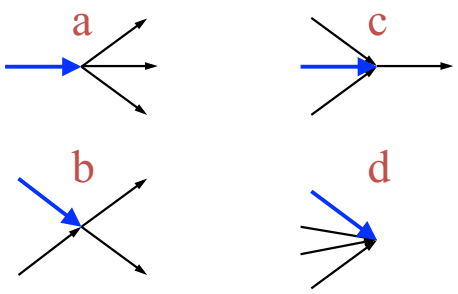

FIG. 4. "Decay" diagrams for a paramagnon. The thick blue line represents the probe paramagnon and the thin black lines represent the heat bath paramagnons.

For example, Fig. 3(c) is a part of the "sunset" diagram. In the diagrammatic series, Fig. 3, we consider only the real part of the sunset diagram. A central point of this work is the consideration the imaginary part of the sunset diagram. However, to extract the most important physics relating to the imaginary part, we will need to consider a different, infinite subseries (see Fig. 9). The following sections are dedicated to this point.

The imaginary part of the self-energy describes broadening:

$$\Gamma_q(\omega) = -\frac{\mathrm{Im}\Sigma_q(\omega)}{\omega},$$
$$G^R(\omega,\mathbf{q}) = \frac{1}{\omega^2-\omega_q^2-\Sigma_q(\omega)} \to \frac{1}{\omega^2-\omega_q^2+i\omega\Gamma_q(\omega)}. \tag{10}$$

There are two points to note: (i) generally, Γ_q depends on ω and hence the line shape can be significantly different from that of a simple Lorentzian; (ii) $\Gamma_q(\omega)$ is an even function of ω since $\mathrm{Im}\Sigma_q(\omega)$ is an odd function. The structure factor corresponding to (10) immediately follows from Eq. (8),

$$S_{\boldsymbol{q}}(\omega) = \frac{1}{\pi(1-e^{-\frac{\omega}{T}})}\left[\frac{\omega\Gamma_q}{\left(\omega^2-\omega_q^2\right)^2+\omega^2\Gamma_q^2}\right]. \tag{11}$$

III. INTUITIVE ANALYSIS AND PERTURBATION THEORY

Let Φ be a paramagnon for which we are determining the decay rate: the "probe paramagnon." The probe paramagnon can spontaneously decay into three paramagnons as shown in Fig. 4(a). In the presence of a heat bath, the probe paramagnon can also scatter from a bath paramagnon—this is the Raman process shown in Fig. 4(b). The fusion process with two or even three heat bath paramagnons is also possible, Figs. 4(c) and 4(d). It is worth noting that the processes in Figs. 4(a), 4(c), and 4(d) are kinematically forbidden for on-mass-shell paramagnons with dispersion (9) [15]. However, one must include the processes in the analysis because close to the Néel temperature, paramagnons are broad and the mass-shell notion is not defined.

Along with each of the above four decay processes, there also exists their inverse process—the "pumping" from the

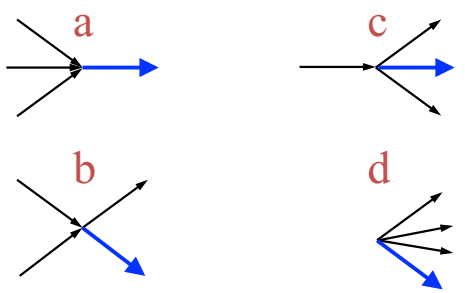

FIG. 5. Diagrams corresponding to pumping (inverse processes) to the paramagnon state. The thick blue line represents the probe paramagnon and the thin black lines represent the heat bath paramagnons.

paramagnon bath shown in Fig. 5. It is intuitively clear that

$$\Gamma_q(\omega) = \Gamma_q^{(d)}(\omega) - \Gamma_q^{(i)}(\omega)\,, \tag{12}$$

where Γ_q is the total width in Eq. (10), $\Gamma_q^{(d)}$ is the decay width associated with processes in Fig. 4 and $\Gamma_q^{(i)}$ is the inverse width associated with processes in Fig. 5. For a formal derivation of (12) see Ref. [19]. Due to the detailed balance, there is a simple relation between the decay and the inverse widths [19,20]:

$$\Gamma_q^{(i)}(\omega) = e^{-\omega/T}\Gamma_q^{(d)}(\omega),$$
$$\Gamma_q(\omega) = (1-e^{-\omega/T})\Gamma_q^{(d)}(\omega). \tag{13}$$

It is interesting to note that while relation (12) is valid for bosons, for fermions $\Gamma = \Gamma^{(d)} + \Gamma^{(i)}$, see Ref. [19].

Now we look at simple perturbation theory, which is equivalent to the Fermi golden rule. Direct application of Fermi golden rule to diagrams in Fig. 4 gives the following decay width:

$$\begin{aligned}\Gamma_q^{(d)}(\omega) = \frac{16(2\pi)^6\mathcal{S}\beta_0^2}{2\omega}\int \frac{d^3k_1}{2\omega_1(2\pi)^3}\frac{d^3k_2}{2\omega_2(2\pi)^3}\frac{d^3k_3}{2\omega_3(2\pi)^3}\\ \times[(1+n_1)(1+n_2)(1+n_3)\,\delta^{(4)}(q-k_1-k_2-k_3)\\ +3n_1(1+n_2)(1+n_3)\,\delta^{(4)}(q+k_1-k_2-k_3)\\ +3n_1n_2(1+n_3)\,\delta^{(4)}(q+k_1+k_2-k_3)\\ +n_1n_2n_3\,\delta^{(4)}(q+k_1+k_2+k_3)].\end{aligned} \tag{14}$$

Here,

$$n_k = \frac{1}{e^{\omega_k/T}-1} \tag{15}$$

is the paramagnon occupation number, and the four-dimensional δ function describes energy and momentum conservation, $\delta^{(4)}(q+k_1+k_2+k_3) = \delta(\omega_q+\omega_1+\omega_2+\omega_3)\delta^{(3)}(\boldsymbol{q}+\boldsymbol{k}_1+\boldsymbol{k}_2+\boldsymbol{k}_3)$. The combinatorial factor $\mathcal{S}$ is due to summation over paramagnon polarizations. For details of calculation of the combinatorial factors see, e.g., Ref. [21]. For a general O(N) group, the factor is

$$\mathcal{S} = 2(N+2). \tag{16}$$

Application of Fermi golden rule to diagrams in Fig. 5 gives the following inverse width:

$$\begin{aligned}\Gamma_q^{(i)}(\omega) = \frac{16(2\pi)^6\mathcal{S}\beta_0^2}{2\omega}\int \frac{d^3k_1}{2\omega_1(2\pi)^3}\frac{d^3k_2}{2\omega_2(2\pi)^3}\frac{d^3k_3}{2\omega_3(2\pi)^3}\\ \times[n_1n_2n_3\,\delta^{(4)}(q-k_1-k_2-k_3)\end{aligned}$$

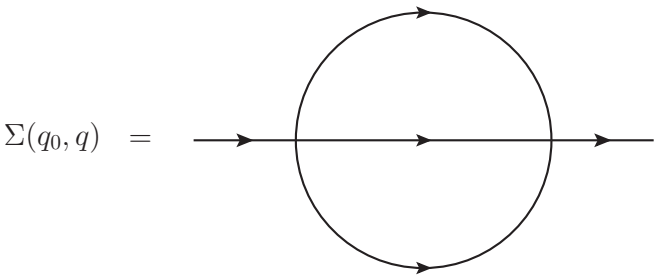

FIG. 6. Matsubara self-energy operator.

$$\begin{aligned}+3(1+n_1)n_2n_3\,\delta^{(4)}(q+k_1-k_2-k_3)\\ +3((1+n_1)(1+n_2)n_3\,\delta^{(4)}(q+k_1+k_2-k_3)\\ +(1+n_1)(1+n_2)(1+n_3)\delta^{(4)}(q+k_1+k_2+k_3)].\end{aligned} \tag{17}$$

Of course, Eqs. (14) and (17) satisfy the relation (13). Hence the full width (13) reads

$$\begin{aligned}\Gamma_q(\omega) = (1-e^{-\omega/T})\frac{16(2\pi)^6\mathcal{S}\beta_0^2}{2\omega}\\ \times\int \frac{d^3k_1}{2\omega_1(2\pi)^3}\frac{d^3k_2}{2\omega_2(2\pi)^3}\frac{d^3k_3}{2\omega_3(2\pi)^3}\\ \times[(1+n_1)(1+n_2)(1+n_3)\,\delta^{(4)}(q-k_1-k_2-k_3)\\ +3n_1(1+n_2)(1+n_3)\,\delta^{(4)}(q+k_1-k_2-k_3)\\ +3n_1n_2(1+n_3)\,\delta^{(4)}(q+k_1+k_2-k_3)\\ +n_1n_2n_3\,\delta^{(4)}(q+k_1+k_2+k_3)].\end{aligned} \tag{18}$$

One can also derive Eq. (18) more formally starting from the Matsubara self-energy operator, see Fig. 6,

$$\begin{aligned}\Sigma(q_0,\boldsymbol{q}) = 16(2\pi)^2\mathcal{S}\beta_0^2T^2\\ \times\sum_{n_1,n_2,n_2=-\infty}^{\infty}\int\int\int\frac{d^3k_1}{(2\pi)^3}\frac{d^3k_2}{(2\pi)^3}\frac{d^3k_3}{(2\pi)^3}\\ \times\frac{(2\pi)^3\delta(\boldsymbol{q}-\boldsymbol{k}_1-\boldsymbol{k}_2-\boldsymbol{k}_3)\delta_{n_0,n_1+n_2+n_3}}{\left(k_{01}^2+\omega_{k_1}^2\right)\left(k_{02}^2+\omega_{k_2}^2\right)\left(k_{03}^2+\omega_{k_3}^2\right)}.\end{aligned} \tag{19}$$

Here, $q_0 = 2\pi T n_0$, $k_{01} = 2\pi T n_1$, $k_{02} = 2\pi T n_2$, $k_{03} = 2\pi T n_3$ are Matsubara frequencies, n_0, n_1, n_2, n_3 are integer numbers. Frequencies ω_{k_i} are given by Eq. (9), $\delta(\boldsymbol{p})$ is the δ function while $\delta_{n,m}$ is the Kronecker symbol. Analytic continuation of (19) from q_0 to real frequency together with Eq. (10) leads to Eq. (18). For full details of the analytic continuation see Refs. [22,23].

IV. ANALYSIS OF QUANTUM DISORDERED AND QUANTUM CRITICAL REGIMES

It is well established that critical two-dimensional quantum antiferromagnets have three different regimes; quantum disordered (QD), quantum critical (QC), and renormalized classical [24]. It is widely assumed, see, e.g., Ref. [4], that analogously there are three different regimes in the disordered part of the phase diagram of a 3D critical antiferromagnet; quantum disordered (QD), quantum critical

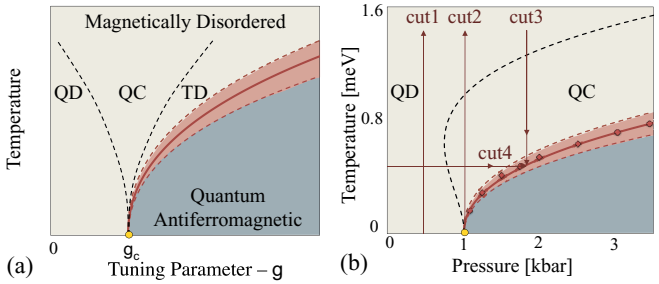

FIG. 7. Two versions of the phase diagram of a 3D quantum antiferromagnet. The Néel temperature curve separates magnetically ordered and magnetically disordered phases. The light red band around the Néel curve indicates the region of dimensional crossover. (a) Commonly accepted phase diagram. The dashed lines in the magnetically disordered phase indicate smooth crossovers between different regimes. (b) The phase diagram derived here to be specific we use parameters of $TlCuCl_3$. The black dashed separates QD and QC regimes. The cuts 1, 2, 3, and 4 are described in the text.

(QC), and thermally disordered (TD). This is schematically illustrated in Fig. 7(a). In this section, we show that logarithmic corrections (running coupling constant) significantly changes this picture.

Diagrams contributing to the running coupling constant and to the self-energy are shown in Figs. 2 and 3. They lead to the following gap equation in the paramagnetic phase [13]:

$$\Delta^2 = \gamma^2(p_c-p)\left[\frac{\beta_\Lambda}{\beta_0}\right]^{\frac{N+2}{N+8}} + 8\pi(N+2)\beta_\Lambda \sum_{\mathbf{k}} \frac{1}{\Omega_{\boldsymbol{k}}}\frac{1}{e^{\frac{\Omega_{\boldsymbol{k}}}{T}}-1},$$
$$\Omega_{\boldsymbol{k}} = \sqrt{k^2+\Delta^2+\Gamma^2}. \tag{20}$$

Here, N corresponds to the O(N) group and β_Λ is the running coupling constant

$$\beta_\Lambda = \frac{\beta_0}{1+\frac{(N+8)\beta_0}{\pi}\ln(\Lambda_0/\Lambda)},$$
$$\Lambda = \max\{\Delta, T\}. \tag{21}$$

Here, Λ_0 is the ultraviolet normalization point. In Eq. (20), we have replaced the general external parameter g to pressure p having in mind further application to $TlCuCl_3$. We will see that in the QD and QC regimes (away from the Neel curve) the width is always small, $\Gamma \ll \Delta$, therefore $\Omega_{\boldsymbol{k}}$ in (20) can be replaced by $\omega_{\boldsymbol{k}}$ determined by Eq. (9).

In the narrow gap limit, $\Gamma \ll \Delta$, which constitutes most of QD and QC regimes, the paramagnon width is determined by the Raman process; see Figs. 4(b) and 5(b). Evaluation of integrals in Eq. (18) gives the following explicit answer:

$$\Gamma_{q=0}(\omega=\Delta) = \frac{\pi\mathcal{S}}{2}\beta_\Lambda^2 T^3 \frac{1-e^{-\Delta/T}}{\Delta^2}\mathcal{I}\left(\frac{\Delta}{T}\right),$$
$$\mathcal{I}(y) = y\frac{6}{\pi^2}\int_y^\infty dx_1 \int_y^{x_1} dx_2\, n_{x_1}(1+n_{x_2})(1+n_{x_3}),$$
$$x_3 = y + x_1 - x_2, \quad n_x = \frac{1}{e^x-1}. \tag{22}$$

In this equation, we substitute the running coupling constant β_Λ instead of β_0 in (18), this substitution accounts for all RG corrections to Eq. (18).

It is also useful to calculate the Fermi golden rule $\Gamma_{q=0}(\omega)$ at arbitrary ω. In this case, generally both the Raman, Figs. 4(b) and 5(b), and the spontaneous, Figs. 4(a) and 5(a), processes contribute. Evaluation of integrals in Eq. (18) gives the following explicit answer:

$$\Gamma_{q=0}(\omega) = \frac{\pi\mathcal{S}}{2}\beta_\Lambda^2 T^3 \frac{1-e^{-\omega/T}}{\omega^2}\left[\mathcal{I}_b\left(\frac{\omega}{T}\right)+\mathcal{I}_a\left(\frac{\omega}{T}\right)\right],$$
$$\mathcal{I}_b(y) = y\frac{6}{\pi^2}\int_{\max\{y_0,2y_0-y\}}^\infty dx_1 \int_{y_0}^{y-y_0+x_1} dx_2$$
$$\times n_{x_1}(1+n_{x_2})(1+n_{x_3})F(x_1,x_2,x_3),$$
$$x_3 = y + x_1 - x_2\,, \quad y_0 = \Delta/T,$$
$$\mathcal{I}_a(y) = \theta(y-3y_0)y\frac{2}{\pi^2}\int_{y_0}^\infty dx_1 \int_{y_0}^{y-y_0-x_1} dx_2$$
$$\times(1+n_{x_1})(1+n_{x_2})(1+n_{x_3})F(x_1,x_2,x_3),$$
$$x_3 = y - x_1 - x_2\,, \quad y_0 = \Delta/T,$$
$$F(x_1,x_2,x_3) = \begin{cases} 1 & \text{if } x_- \leqslant x_3 \leqslant x_+ \\ 0 & \text{otherwise} \end{cases},$$
$$x_- = \sqrt{\left(\sqrt{x_1^2-y_0^2}-\sqrt{x_2^2-y_0^2}\right)^2+y_0^2},$$
$$x_+ = \sqrt{\left(\sqrt{x_1^2-y_0^2}+\sqrt{x_2^2-y_0^2}\right)^2+y_0^2}. \tag{23}$$

Of course, at $\omega=\Delta$, Eq. (23) coincides with Eq. (22). It is worth noting that the coupling β_Λ runs with energy scale $\Lambda = \max\{\sqrt{\omega^2-q^2}, T\}$.

A. Quantum disordered regime

Consider cut1 in the QD regime of the phase diagram, Fig. 7(b). At low temperatures, deep in the QD regime where $e^{-\Delta/T} \ll 1$, the gap determined by Eq. (20) is practically equal to its value at zero temperature. Direct evaluation of the integral in Eq. (22) gives

$$\frac{\Gamma_{q=0}(\omega=\Delta)}{\Delta} = \frac{3\mathcal{S}}{\pi}\beta_\Lambda^2\frac{T^2}{\Delta^2}e^{-\Delta/T} \ll 1\,. \tag{24}$$

B. Quantum critical regime

To address the QC regime, let us tune to the critical point by setting $g=g_c$ and increase the temperature along cut 2 in Fig. 7(b). The solution of Eq. (20) in this situation reads

$$\Delta = T\sqrt{\frac{2(N+2)\pi\beta_\Lambda}{3}}\,\Theta(\beta_\Lambda)\,. \tag{25}$$

The scaling function Θ is nonanalytic at $\beta\to 0$, $\Theta(\beta) = (1-\sqrt{\frac{3(N+2)\beta}{2\pi}}+\cdots)$, and therefore deviates from unity noticeably even at small values of the coupling constant. The plot of $\Theta(\beta)$ with $N=3$ is shown in Fig. 8. Hence, using Eqs. (22) and (25), we find

$$\frac{\Gamma_{q=0}(\omega=\Delta)}{\Delta} = \frac{3\mathcal{S}}{4(N+2)}\beta_\Lambda\,\Phi(\beta_\Lambda)\,. \tag{26}$$

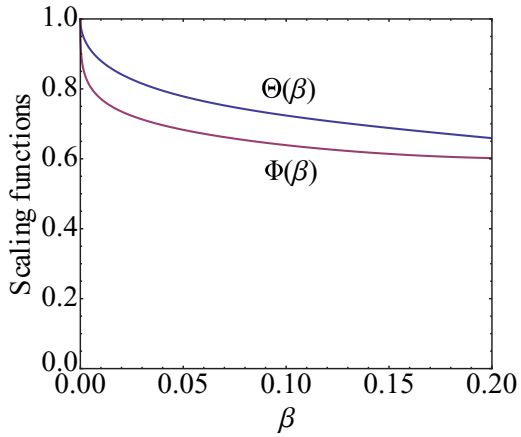

FIG. 8. Scaling functions $\Theta(\beta)$ and $\Phi(\beta)$ in Eqs. (25) and (26) for $N = 3$.

Similar to Θ, the scaling function Φ, normalized as $\Phi(0) = 1$, is nonanalytic in β. The plot of $\Phi(\beta)$ is presented in Fig. 8. As expected, both Δ, Eq. (25), and Γ, Eq. (26), scale linearly with temperature along cut 2. However, there is also a logarithmic dependence related to the coupling constant. The dependencies of Δ and Γ on the coupling constant are significantly different. In a very close vicinity of QCP, $T \to 0$, the coupling constant (21) is logarithmically approaching zero. Therefore here $\Gamma \ll \Delta \ll T$. However, the coupling constant grows with raising temperature and reaches the crossover value β_c where $\Gamma \ll \Delta = T$. The value of β_c immediately follows from Eq. (25); for $N = 3$, it is $\beta_c \approx 0.23$, and here $\Gamma/\Delta \approx 0.21$. The crossover value of β is sufficiently small, so our approach is justified.

C. Crossovers and contours

One can define the crossover line between QD and QC regimes by the equality

$$\Delta(g,T) = T\ . \tag{27}$$

In the QD regime, $\Delta > T$, and in the QC regime, $\Delta < T$. The crossover line found from Eq. (20) is shown in Fig. 7(b) by the black dashed line. It is different from the simple power scaling indicated in Fig. 7(a). Technically the difference is due to the logarithmic running of the coupling constant. Physically, we say that this difference is due to the system being at its upper critical dimension where there are two energy scales; the infrared scale, which is equal to temperature, and the ultraviolet one, which is determined by the position of the Landau pole, see discussion in Ref. [13]. As discussed in the previous paragraph, the crossing point between the black crossover line and cut 2 of Fig. 7(b) corresponds to $\beta = \beta_c$.

Let us consider now the cut 3 in Fig. 7(b), which traces from the QD regime down to the Néel phase transition. Along this cut, the ratio Δ/T is monotonically decreasing from $\Delta/T \geqslant 1$ above the QD to QC crossover, to $\Delta/T = 0$ at the transition. Meanwhile, the ratio Γ/Δ is monotonically increasing. We do not see any fingerprints of a crossover to the "thermally disordered" regime. From our analysis of the static and dynamic properties, we conclude that separately defining a thermally disordered regime brings no extra meaning to the phase diagram. On the other hand, in the very close vicinity of the Néel temperature, the ratio Γ/Δ becomes equal to unity, and as such brings about a very distinct regime. This regime corresponds to the dimensional crossover to the "classical critical" regime indicated by the light red band in Fig. 7(b). Our next goal is to describe this crossover.

V. DECAY WIDTH EXPRESSED IN TERMS OF THE SPECTRAL FUNCTION. THE GOLDEN RULE OF QUANTUM KINETICS

Our analysis in previous sections and in particular the derivation of Eq. (18) is based on two grounds: (i) the coupling constant is small, $\beta \ll 1$, so as to justify the applied perturbation theory; (ii) the paramagnon broadening is small compared to the energy, $\Gamma \ll \Delta$, so that the notion of the thermal occupation number (15) is well defined. Close to the Néel temperature point (ii) is not valid. While the coupling constant is still small, paramagnons become relatively broad as is clearly indicated by experiment [1]. Note: "broad" here means that the width is comparable or larger than the gap. Physically, the paramagnons are broad near the Néel temperature because their gap, Eq. (9), approaches zero as $T \to T_N$. This is the overdamped regime or the "hot quantum soup." In this regime, Eqs. (15) and (18) do not make physical sense since a quasiparticle description is not well defined. Note that quasiparticles with large momentum are still well defined, $\Gamma_q(\omega = \omega_q) \ll \omega_q$ for sufficiently large q. The Bose-Einstein occupation number, as presented in Eq. (15), explicitly assumes the quasiparticles to be on mass shell; $\omega = \omega_{\boldsymbol{q}} = \sqrt{\boldsymbol{q}^2 + \Delta^2}$. However, for broad quasiparticles, their dispersion could (crudely speaking) lay anywhere in the range $\omega_{\boldsymbol{q}} - \Gamma/2 < \omega < \omega_{\boldsymbol{q}} + \Gamma/2$. It is in this sense that the quasiparticle description is not valid. With these considerations in mind, our goal is to develop a theory for the regime of large heat bath scattering and subsequent large uncertainty in the quasiparticle occupation numbers. We call this the "hot quantum soup" regime, which corresponds to the crossover to the classical critical regime. We do not use the terminology "classical critical," which is appropriate to underline the dimensional crossover; 4D $\to$ 3D, and with it, the unimportance of time. Instead, we use the term "hot quantum soup" to underline the broadening and overdamped dynamics of paramagnons.

To achieve our goal, we first dispense with the Bose-Einstein occupation numbers, and rewrite (18) in terms of spectral functions. In the small width regime, point (ii) above, the imaginary part of the retarded Green's function follows from Eq. (4),

$$-\frac{1}{\pi}\mathrm{Im}\, G^R(\omega,\boldsymbol{q}) = \frac{1}{2\omega_q}[\delta(\omega-\omega_q) - \delta(\omega+\omega_q)]. \tag{28}$$

Combining this with (8), we find

$$S_{\boldsymbol{q}}(\omega) = \frac{1}{2\omega_q}[(1+n_q)\delta(\omega-\omega_q) + n_q\delta(\omega+\omega_q)]. \tag{29}$$

One can also derive this directly by applying the Fermi golden rule to the interaction given by the external source (6). The first term in brackets in Eq. (29) describes the creation of a magnon by the external source, while the second term in

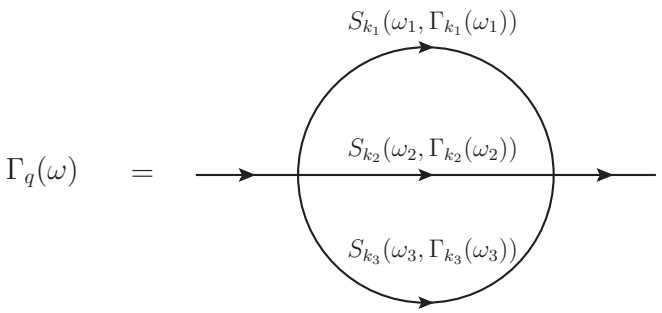

FIG. 9. Diagrammatic illustration of Dyson equation describing the golden rule of quantum kinetics.

brackets describes a magnon being absorbed from the heat bath by the external source. It is easy to check that using (29) the width (18) can be rewritten as

$$\Gamma_q(\omega) = \mathcal{S}(8\pi)^2\beta^2\frac{(1-e^{-\omega/T})}{2\omega}\int S_{\boldsymbol{k}_1}(\omega_1)S_{\boldsymbol{k}_2}(\omega_2)S_{\boldsymbol{k}_3}(\omega_3) \times (2\pi)^4\delta(\omega-\omega_1-\omega_2-\omega_3)\delta(\boldsymbol{q}-\boldsymbol{k}_1-\boldsymbol{k}_2-\boldsymbol{k}_3) \times \frac{d\omega_1 d^3k_1}{(2\pi)^3}\frac{d\omega_2 d^3k_2}{(2\pi)^3}\frac{d\omega_3 d^3k_3}{(2\pi)^3}\,. \tag{30}$$

An important point is that we can use the general expression (11) for the structure factor, such that in this form (30) does not contain occupation numbers. The expression is valid for quasiparticles of arbitrary broadness. In particular, it is valid in the "hot quantum soup" regime where quasiparticles are poorly defined, $\Gamma \gtrsim \omega$. We call the combinations of these two equations, Eqs. (30) and (11), the golden rule of quantum kinetics.

Self-consistent solution of Eqs. (30) and (11) is a Dyson-equation-like procedure to determine $S_{\boldsymbol{q}}(\omega,\Gamma_{\boldsymbol{q}})$. Diagrammatically, the Dyson equation is illustrated in Fig. 9. Most importantly, the solution of the golden rule of quantum kinetics gives the structure factor, which can be directly compared with experiment. Note that Fig. 9 is not a usual Feynman/Matsubara diagram; the lines in Fig. 9 represent structure factors as opposed to Green's functions. We also comment that Eq. (29) is used to derive (30) in the narrow line regime, $\Gamma \to 0$. However, as soon as one wishes to go beyond simple perturbation theory, and account for the back influence of the decay width on the decay phase space, then Eq. (29) becomes invalid (generally), and it is Eqs. (30) and (11) that are to be solved self-consistently.

Now we can comment on the general structure of our theory and compare with other approaches. In essence, we perform summations of infinite chains of diagrams. The chains of diagrams; those for the real part of the self-energy and those for the imaginary part of the self-energy, are different. The different chains are dictated by different physics: the real part is dominated by logarithmic ultraviolet/infrared physics and is related to the logarithmic running coupling constant, see discussion after Eq. (9), while the imaginary part, Eq. (30), in the overdamped regime, is dominated by the power-divergent, infrared physics. These two different summations cannot be represented as a summation of a single infinite set of Matsubara diagrams since within the Matsubara technique, the real part and the imaginary part are treated on an equal footing. And as far as we understand, Eq. (30) cannot be represented within any standard diagrammatic technique.

One of the central points of the present work is self-consistent Eq. (30) for the spectral function/width. The equation takes care of the infrared, power divergence in the overdamped regime. The following points are crucial for the understanding and justification of our approach.

(i) We assume proximity to the quantum critical point. The proximity implies that the logarithmically running coupling constant is sufficiently small to justify truncation of diagrams, $\beta_q \ll 1$.

(ii) When approaching the Neel temperature, the perturbation theory for the imaginary part breaks down; the width naively calculated using the sunset diagram (analytical continuation of Matsubara) is diverging. This is an infrared power divergence. The failure of the perturbative approach is not a result of the coupling constant becoming large, instead, the perturbative approach fails because the gap (=mass) becomes small. The small gap implies the overdamped regime.

(iii) Away from the Neel temperature, Eq. (30) is equivalent to the simple perturbation theory (Fermi golden rule), it gives the same width as straightforward analytical continuation of the sunset Matsubara diagram.

(iv) The RG procedure accounts only for the *on mass-shell* contribution to the real part of the sunset self-energy. However, in our evaluation of the imaginary part of the self-energy using Eqs. (30) and (11), we consider both the *on* and *off mass-shell* contributions. To subsequently find the off mass-shell contribution to the real part of the self-energy, one can exploit the analytic properties, i.e., Kramers-Kronig relation. This extra step is beyond what is presented in the text, instead, the calculation is performed in Appendix. As expected, the off mass-shell energy-dependent contribution is negligibly small. Furthermore, away from the Neel temperature/overdamped regime, one does not need to consider the off mass-shell contribution at all.

There are approaches to the thermal field theory that are based on uncontrolled truncations of Matsubara diagrams, see, e.g., Refs. [25,26]. These works do not rely on proximity to a QCP, therefore the coupling constant is, without prior knowledge, large and the truncations uncontrolled. This is not the case in the present work, see point (i) above. Besides that, as already explained, our technique in principle cannot be reduced to a summation of series of Matsubara diagrams.

VI. MATHEMATICAL ANALYSIS OF THE GOLDEN RULE OF QUANTUM KINETICS

In this section, we provide a general mathematical analysis of the golden rule of quantum kinetics, without reference to any particular system. Our aim is to illustrate the necessity of the nonperturbative resummation of the imaginary part, i.e., the self-consistent solution of Eqs. (30) and (11). To this end, we disregard the RG running of the coupling constant and set it to

$$\beta = 0.2. \tag{31}$$

In the next section, we will again account for the RG running.

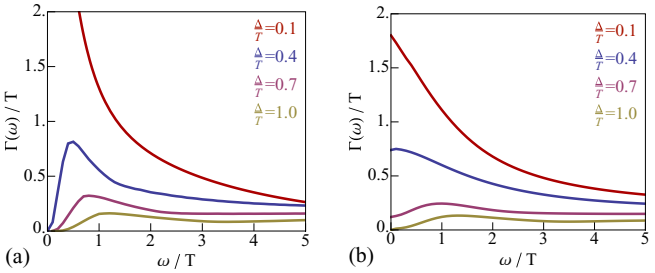

FIG. 10. Paramagnon width function at zero momentum, $\Gamma_{q=0}(\omega)$, vs frequency. The function is calculated with the coupling constant (31) for different values of the gap Δ. (a) Obtained using the simple Fermi golden rule, Eq. (18). (b) Obtained using the golden rule of quantum kinetics; Eqs. (30) and (11).

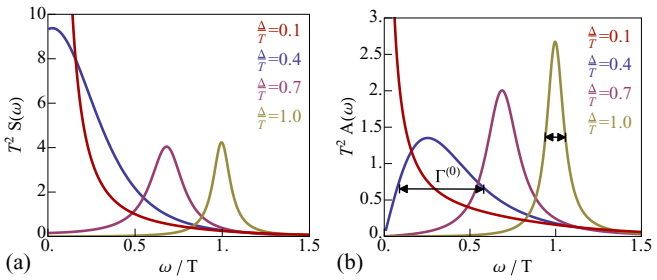

FIG. 11. (a) The structure factor $T^2 S_{q=0}(\omega)$ vs frequency for different values of the gap Δ. (b) The spectral density $A_{q=0}(\omega) = -\frac{1}{\pi}\mathrm{Im}G^R(\omega, q=0)$ vs frequency for different values of the gap Δ. Both $S_{q=0}(\omega)$ and $A_{q=0}(\omega)$ correspond to $\Gamma_{q=0}(\omega)$ (solid lines) in Fig. 10.

Fortunately, the most singular integrations in Eq. (30) can be performed analytically. To avoid long equations here, we present the answer only for $q = 0$:

$$\Gamma_{q=0}(\omega) = \frac{\mathcal{S}\beta^2}{\pi}\frac{(1-e^{-\omega/T})}{\omega}\int_{-\infty}^{+\infty} d\omega_1 d\omega_2 \int_0^{+\infty} dk_1^2 dk_2^2 \times \int_{(k_1-k_2)^2}^{(k_1+k_2)^2} dk_3^2\, S_{\boldsymbol{k}_1}(\omega_1) S_{\boldsymbol{k}_2}(\omega_2) S_{\boldsymbol{k}_3}(\omega-\omega_1-\omega_2). \tag{32}$$

Numerical evaluation of this expression is straightforward. Consider cut 3 in Fig. 7(b); we approach the Néel temperature from the QC regime. Along this cut it is convenient to use temperature as the energy scale, and have ω/T, Γ_q/T, Δ/T, and q/T as dimensionless variables. We remind the reader that paramagnon speed is set to unity, $c = 1$, and hence $q \to cq$ has dimension of energy. To illustrate the use of the golden rule of quantum kinetics, and to contrast with the usual Fermi golden rule, we present Fig. 10, which shows plots of the paramagnon width function $\Gamma_{q=0}(\omega)$ versus ω for values of Δ/T ranging from $\Delta/T = 1$ to $\Delta/T = 0.1$. The width function $\Gamma_{q=0}(\omega)$ calculated using the Fermi golden rule (18) is shown in Fig. 10(a), while the width function calculated using the golden rule of quantum kinetics, i.e., by iterative solution of Eqs. (30) and (11), is shown in Fig. 10(b). Of course, at small Γ/Δ, which here corresponds to large Δ, $\Delta/T \gtrsim 1$, the two methods must reduce to the same result, and they do so, as is evident from Fig. 10. They also give the same result at large values of ω. On the other hand at small values of Δ and small ω the results are very different. This is not surprising since the Fermi golden rule assumes the on-mass-shell notion related to Eq. (15), the notion and the Fermi golden rule fails at sufficiently small values of Δ/T where the width is very large, $\Gamma/\Delta > 1$. In particular, this results in a formal divergence of Γ in the limit $\omega, \Delta \to 0$. On the other hand, the golden rule of quantum kinetics does not require the on-mass-shell notion and therefore does not suffer from the artificial divergence. For the remainder of our analysis, we will use only the golden rule of quantum kinetics.

The structure factor $S_{\boldsymbol{q}}(\omega)$, as given by Eq. (11), provides a direct physical link to experiment. In Fig. 11(a), we present the structure factors $S_{q=0}(\omega)$, which correspond to the widths $\Gamma_{q=0}(\omega)$ as given in Fig. 10 by solid lines. The structure factor has dimension [energy]$^{-2}$, therefore similar to other variables in the QC regime we use the appropriate power of temperature to balance dimension, $S \to T^2 S$. To supplement the results shown in Fig. 11(a). In Fig. 11(b), we present plots of the spectral density, $A_{\boldsymbol{q}}(\omega) = -\frac{1}{\pi}\mathrm{Im}G^R(\omega, \boldsymbol{q})$. The spectral density $A(\omega)$ is related to the structure factor according to Eq. (8). The spectral density has been used experimentally to determine effective line widths. In the present analysis, we define $\Gamma_q^{(0)}$ to be the FWHM of the spectral density, which is indicated by the doubled-headed, arrowed lines in Fig. 11(b). We stress that $\Gamma_q^{(0)}$ has no ω dependence, but it depends on the gap Δ, momentum $\boldsymbol{q}$, and temperature T.

At sufficiently small values of Δ/T the definition of $\Gamma^{(0)}$ as FWHM of the spectral density practically does not make sense, the $A(\omega)$ becomes hugely asymmetric, see the $\Delta/T = 0.1$ curve in Fig. 11(b). This corresponds to the crossover to the overdamped regime, or in other words to the crossover from quasiballistic dynamics to the fully diffusive one. The crossover value of Δ_c depends on the value of the running coupling constant β_Λ. The smaller values of β_Λ correspond to the smaller Δ_c/T. All the available experimental data for $TlCuCl_3$ are in the regime of reasonably well defined $\Gamma^{(0)}$.

VII. COMPARISON WITH EXPERIMENTAL DATA ON $TlCuCl_3$

The widths of paramagnons $\Gamma_{q=0}^{(0)}$ in $TlCuCl_3$ have been measured via inelastic neutron scattering [1]. The data is obtained for various values of Δ and T, spanning the entire phase diagram Fig. 1. To compare our theory with the data we need to set $N = 3$ and specify parameters Λ_0 and β_0 in the running coupling constant (21) as well as γ and p_c in (20). The value of Λ_0 is arbitrary as soon as it is below the position of the Landau pole, and the value of β_0 depends of the particular system/compound and on the value of Λ_0. An analysis of the $TlCuCl_3$ data performed in Ref. [13] shows that for this compound

$$\beta_0 = 0.23 \quad \text{for} \quad \Lambda_0 = 1 \text{ meV};$$
$$p_c = 1.01 \text{ kbar} \quad \gamma = 0.68 \text{ meV/kbar}^{1/2}. \tag{33}$$

Note that the analysis [13] does not include paramagnon widths. It based solely on the phase diagram and on the data on values of the quasiparticle gaps.

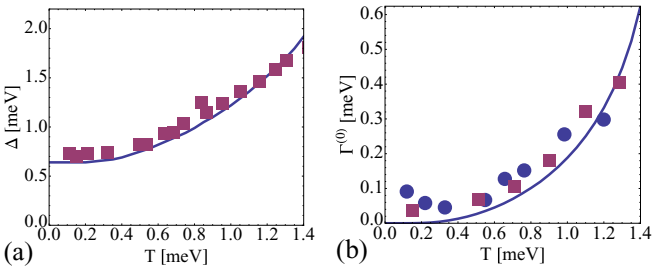

FIG. 12. The gap (a) and the width (b) in $TlCuCl_3$ along the cut1 in the phase diagram Fig. 7(b). We take the cut at $p = 0$ kbar. Squares and circles represent experimental data [27] and the theory is shown by lines.

Using parameters (33) and the theory developed in the present work we can calculate gaps. Let us first consider the cut 1 in Fig. 7(b) and put it at zero pressure pressure position, $p = 0$. The gap and the width along this cut are plotted in Fig. 12. Squares and circles represent experimental data [27] and theory is shown by lines. The gap is determined by Eq. (20) and the width by Eq. (22). [Note that Eq. (24) is not sufficient since it is valid only in the regime $\exp(-\Delta/T) \ll 1$.] The agreement between experiment and theory for the gap is not surprising, the experimental gap was used in Ref. [13] to determine the parameters (33). Most important, the agreement for the width is remarkable.

Next we consider the cut 2 in Fig. 7(b), the quantum critical regime. The gap and the width along this cut are plotted in Fig. 13. Squares represent experimental data [1] and theory is shown by lines. The gap is determined by Eq. (25) and the width by Eq. (26) Again, the agreement between experiment and theory is remarkable.

Now we consider cuts 3 and 4 in Fig. 7(b). This cuts approach the Neel temperature and hence the "simple" RG used for cuts 1 and 2 is not sufficient. We need RG plus the golden rule of quantum kinetics, Eqs. (30) and (11). In the vicinity of the Neel temperature, spectral lines become asymmetric and hence the definition of width becomes ambiguous. We use values of $\Gamma^{(0)}$ defined in Sec. VI. In evaluating Eq. (30), the coupling β_Λ formally runs with energy scale $\Lambda = \max\{\sqrt{\omega^2 - q^2}, T\}$, yet we use $\Lambda = \max\{\Delta, T\}$, which makes a negligible difference Ref. [28].

In Fig. 14, we present theoretical and experimental values of the width $\Gamma^{(0)}_{q=0}$ and the gap Δ. Panel (a) corresponds to the vertical cut 3 in Fig. 7(b); temperature varies at fixed pressure, $p = 1.75$ kbar. Panel (b) corresponds to the horizontal cut 4 in Fig. 7(b); pressure varies at fixed temperature, $T = 0.5$ meV. Agreement between theoretical and experimental widths presented in Fig. 14(a) is very good. This includes the highly nontrivial, hot quantum soup regime close to the Néel temperature where the width calculated via the golden rule of quantum kinetics is different from that calculated via the simple Fermi golden rule. On the other hand, Fig. 14(b) demonstrates a disagreement between theory and experiment about factor 2 in the theoretically "simple" interval $0 < p < p_c$. In principle, one can refer the disagreement to impurities. However, it is unlikely since the agreement at endpoints of this interval, $p = 0$, Fig. 12 and at $p = p_c$, Fig. 13, is excellent. The reason for the disagreement remains unclear to us.

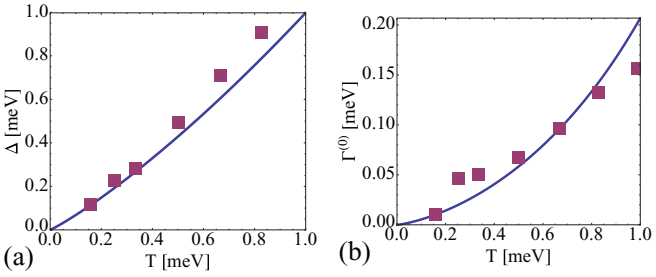

FIG. 13. The gap (a) and the width (b) in $TlCuCl_3$ along the critical cut 2, $p = p_c$, in the phase digram Fig. 7(b). Squares represent experimental data [1] and the theory is shown by lines.

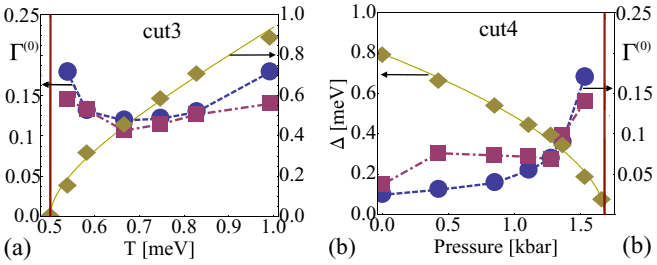

FIG. 14. Theoretical and experimental values of the width $\Gamma^{(0)}_{q=0}$ and the gap Δ. Panel (a) corresponds to the vertical cut 3 in Fig. 7(b), temperature varies at fixed pressure, $p = 1.75$ kbar. Panel (b) corresponds to the horizontal cut 4 in Fig. 7(b), pressure varies at fixed temperature, $T = 0.5$ meV. In both panels, blue circles show theoretical results of the present work, while magenta squares show experimental results of Ref. [1]. Yellow diamonds show experimental results for the gap [1]. Dashed blue and magenta as well as solid yellow lines connecting the points are given just for guidance.

Finally, to complete this section, in Fig. 15, we present the phase diagram of $TlCuCl_3$ with lines of constant Γ/Δ. At large T where the running coupling constant becomes large the

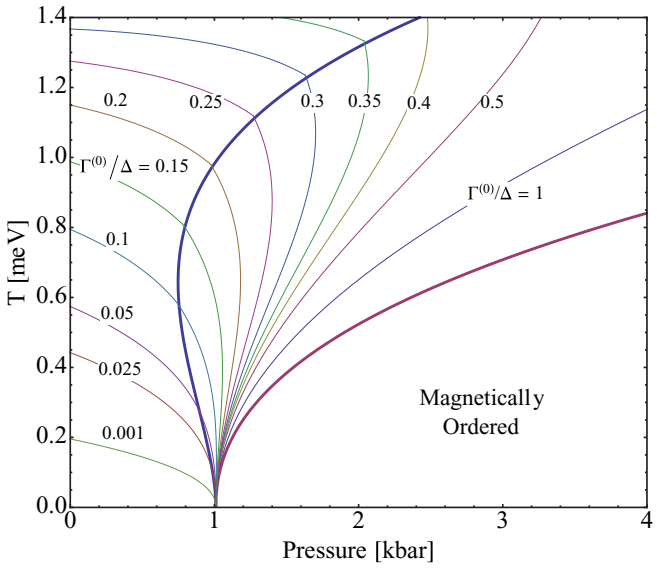

FIG. 15. Contours of $\Gamma^{(0)}/\Delta$ on the phase diagram of $TlCuCl_3$. Thick red line is T-Neel, thick blue line is QD/QC crossover. All other curves are traces of constant $\Gamma^{(0)}/\Delta$.

lines have small cusps at the QD/QC crossover line (i.e., when $\Delta = T$). Of course the cusps are byproducts of the logarithmic RG where the argument is $\ln(\max\{\Delta, T\})$. The magnitude of the cusp indicates the inaccuracy of the RG approach at a given temperature. One can consider the line $\Gamma/\Delta = 1$ as crossover from the dilute gas to the hot quantum soup regime.

There are two comments in conclusion of this section. (i) Our calculation of widths has no adjustable fitting parameters. All parameters were taken from an independent analysis Ref. [13], which made no reference to decay widths. (ii) Calculations performed in this section do not take into account the small anisotropy which exists in $TlCuCl_3$. It relatively straightforward to account for the anisotropy via introduction of an additional anisotropic effective mass as is discussed in Refs. [10,13]. We have performed such a calculation and checked that the anisotropy does not influence the widths presented in Figs. 12–14 beyond a few percent.

VIII. CONCLUSIONS

We analyze the magnetically disordered phase of 3D quantum antiferromagnets. Motivated by observed kinetics of paramagnons in quantum antiferromagnet $TlCuCl_3$, our analysis is concerned with the nonequilibrium properties: paramagnon lifetimes and the neutron scattering structure factor. (i) We show that logarithmic running of the coupling constant in the upper critical dimension changes the commonly accepted picture of the quantum disordered and quantum critical regimes. (ii) We calculate paramagnon decay widths in quantum critical and quantum disordered regimes. (iii) Close to the Neel temperature the paramagnon width becomes comparable to its energy and falls into the hot quantum soup regime where the quasiparticle lifetimes are very short due to multiple scattering from other quasiparticles. To describe the "soup," we develop a new finite frequency, finite temperature technique for a nonlinear quantum field theory; the golden rule of quantum kinetics. The formulation is generic and applicable to any quantum field theory with weak coupling. (iv) Comparing with data on $TlCuCl_3$, we find an excellent agreement between theory and experiment.

In the challenging field of many-body quantum systems, a novel technical approach can often help illuminate the physical problem at hand. In this paper, we developed a formalism that offers a novel means to calculating nonequilibrium properties of 3+1 dimensional, critical quantum antiferromagnets. Our analysis provides an economical representation, and we hope that the formalism presented here could be applied to other systems of this kind; for example, a wide class of spin dimerised magnetic models.

ACKNOWLEDGMENTS

We thank C. Ruegg, and Y. Kharkov for important comments and discussions. We are especially grateful to B. Normand for critical reading of the manuscript. The work has been supported by the Australian Research Council, Grants No. DP110102123 and No. DP160103630.

APPENDIX: NON-RG CONTRIBUTION TO THE REAL PART OF THE SELF-ENERGY

In the main text, we self-consistently solve the golden rule of quantum kinetics, Eqs. (11) and (29), to find the imaginary part of the self-energy as well as the structure factor. In doing so, we ignore the small frequency dependence of the real part of the self-energy, $\Re\Sigma_q(\omega)$. Our approximation is equivalent to taking $\Re\Sigma_q(\omega) \approx \Re\Sigma_q(\Delta_0)$, where Δ_0 is the physical mass calculated using RG. In this appendix, we take into account the full frequency dependence of the real part of the self-energy. This is achieved by adding the frequency-dependent correction to the mass gap, $\delta\Sigma(\omega) \equiv \Re\Sigma_q(\omega) - \Re\Sigma_q(\Delta_0)$, and solving the following set of equations self-consistently:

$$\Delta^2(\omega) = \Delta_0^2 + \delta\Sigma(\omega), \tag{A1}$$

$$\Gamma_q(\omega) = -\frac{\Im\Sigma_q(\omega)}{\omega}, \tag{A2}$$

$$A_{\boldsymbol{q}}(\omega) = \frac{1}{\pi}\left\{\frac{\omega\Gamma_q(\omega)}{[\omega^2 - (q^2 + \Delta^2(\omega))]^2 + \omega^2\Gamma_q^2(\omega)}\right\}. \tag{A3}$$

Here, $\Gamma_q(\omega)$ is defined as in the main text Eq. (30), the spectral density $A_q(\omega) \equiv (1 - e^{-\omega/T})S_q(\omega)$, while the real part is

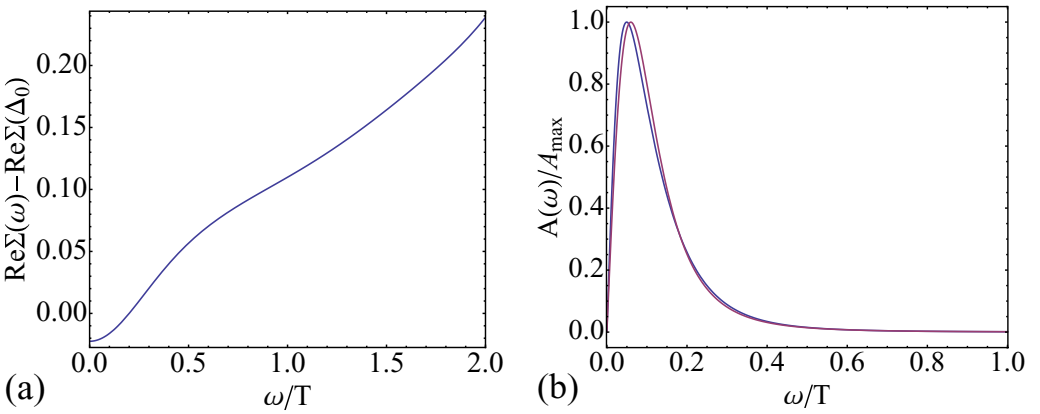

FIG. 16. (a) Frequency-dependent correction to mass gap; the non-RG contribution to the real part of self-energy. (b) The (normalized) spectral density $A_{q=0}(\omega)$. (Blue curve) Including the non-RG, frequency-dependent correction; (maroon curve) excluding the non-RG, frequency-dependent correction.

found via analytic properties (Kramers-Kronig relation):

$$\Re\Sigma_q(\omega,T) = \frac{1}{\pi}\mathcal{P}\int_{-\infty}^{+\infty}\frac{\Im\Sigma_q(\omega',T)}{\omega'-\omega}d\omega' = \frac{1}{\pi}\mathcal{P}\int_{-\infty}^{+\infty}\frac{-\omega'\Gamma_q(\omega')}{\omega'-\omega}d\omega'. \quad \text{(A4)}$$

Here we ignore momentum dependence, which would give some small additional correction. Since we already know $\Gamma_q(\omega)$ from solving the golden rule of quantum kinetics, we can use the Kramers-Kronig relation (A4) to evaluate the real part. The results are shown in Fig. 16 for the data point $\{\Delta_0,T\} = \{0.2,0.5\}$ meV, with coupling constant $\beta = 0.15$. Figure 16(a) shows the frequency dependence of the non-RG contribution to the real part of the self-energy. Figure 16(b) shows the spectral density with and without inclusion of the frequency-dependent real part of self-energy, blue and maroon curves, respectively. We see that the inclusion of the real part has a negligible influence.

[1] P. Merchant, B. Normand, K. W. Kramer, M. Boehm, D. F. McMorrow, and Ch. Ruegg, Nat. Phys. **10**, 373 (2014).

[2] Ch. Rüegg, B. Normand, M. Matsumoto, A. Furrer, D. F. McMorrow, K. W. Krämer, H. U. Güdel, S. N. Gvasaliya, H. Mutka, and M. Boehm, Phys. Rev. Lett. **100**, 205701 (2008).

[3] O. P. Sushkov, Nat. Phys. **10**, 339 (2014).

[4] S. Sachdev, *Quantum Phase Transitions* (Cambridge University Press, Cambridge, 2011).

[5] A. B. Harris, D. Kumar, B. I. Halperin, and P. C. Hohenberg, Phys. Rev. B **3**, 961 (1971).

[6] S. Tŷc and B. I. Halperin, Phys. Rev. B **42**, 2096 (1990).

[7] P. Kopietz, Phys. Rev. B **41**, 9228 (1990).

[8] S. P. Bayrakci, D. A. Tennant, Ph. Leininger, T. Keller, M. C. R. Gibson, S. D. Wilson, R. J. Birgeneau, and B. Keimer, Phys. Rev. Lett. **111**, 017204 (2013).

[9] M. E. Zhitomirsky and A. L. Chernyshev, Rev. Mod. Phys. **85**, 219 (2013).

[10] Y. Kulik and O. P. Sushkov, Phys. Rev. B **84**, 134418 (2011).

[11] Y. Q. Qin, B. Normand, A. W. Sandvik, and Z. Y. Meng, Phys. Rev. B **92**, 214401 (2015).

[12] I. Affleck and G. F. Wellman, Phys. Rev. B **46**, 8934 (1992).

[13] H. D. Scammell and O. P. Sushkov, Phys. Rev. B **92**, 220401(R) (2015).

[14] E. M. Lifshitz and L. P. Pitaevskii, *Statistical Physics II* (Pergamon Press, Oxford, 1980).

[15] Note that in the ordered phase spontaneous decay of a magnon is generally allowed. For an analysis at zero temperature, we draw the readers attention to the work of Refs. [16–18].

[16] M. Mourigal, M. E. Zhitomirsky, and A. L. Chernyshev, Phys. Rev. B **82**, 144402 (2010).

[17] M. E. Zhitomirsky and A. L. Chernyshev, Phys. Rev. Lett. **82**, 4536 (1999).

[18] Y. T. Katan and D. Podolsky, Phys. Rev. B **91**, 075132 (2015).

[19] H. A. Weldon, Phys. Rev. D **28**, 2007 (1983).

[20] J. F. Donoghue and B. R. Holstein, Phys. Rev. D **28**, 340 (1983).

[21] M. E. Peskin and D. V. Schroeder, *An Introduction To Quantum Field Theory*, Frontiers in Physics (Westview, Boulder, CO, 1995), Chap. 11.

[22] De-fu Hou and Jia-rong Li, Commun. Theor. Phys. **26**, 125 (1996).

[23] P. D. Pisarski, Nucl. Phys. B **309**, 476 (1988).

[24] S. Chakravarty, B. I. Halperin, and D. R. Nelson, Phys. Rev. B **39**, 2344 (1989).

[25] H. van Hees and J. Knoll, Phys. Rev. D **65**, 025010 (2001).

[26] H. van Hees and J. Knoll, Phys. Rev. D **65**, 105005 (2002).

[27] Ch. Rüegg, B. Normand, M. Matsumoto, Ch. Niedermayer, A. Furrer, K. W. Krämer, H.-U. Güdel, Ph. Bourges, Y. Sidis, and H. Mutka, Phys. Rev. Lett. **95**, 267201 (2005).

[28] For off-mass shell four-momentum $\mu^2 = \omega^2 - q^2 \neq \Delta^2$, the only significant contribution to Eq. (30) comes from the "window" $\mu^2 \approx \Delta^2 \pm \Gamma^2$, since integrand (30) is heavily suppressed otherwise. In the limit $\Delta \ll T, \Gamma > \Delta$, but the running scale will be set by $\Lambda = \max\{\mu, T\} = T$. In the opposite limit $\Delta \gg T$, then $\Gamma \ll \Delta$ since $\Gamma \sim e^{-\Delta/T}$ (see Sec. IV) and the running scale is essentially unaffected; $\Lambda^2 \approx \Delta^2 \pm \Gamma^2 \approx \Delta^2$.